Digest Journal of Nanomaterials and Biostructures Vol. 6, No 2, April-June 2011, p. 391-402

EFFECTS OF ELECTRODE ARRAY DIMENSIONS ON THE PUMPING PERFORMANCE OF TRAVELING-WAVE ELECTRO-OSMOTIC MICRO-PUMPS

JAUH-SHYONG CHEN[a], KAO-FENG YARN[b], SHIH-FENG CHENG[a], WIN-JET LUO[a,*], MENG-HUA CHUNG[a]
[a]*Department of Refrigeration, Air Conditioning and Energy Engineering, National Chin-Yi University of Technology, Taichung County, Taiwan 411, ROC*
[b]*Department of Electronic Engineering, Far East University, Tainan, Taiwan 744, ROC*

This study includes a series of numerical simulations to investigate the pumping performance of electroosmotic micro-pumps that contained electrode arrays patterned on one side of a micro-channel. The simulations were used to investigate the effects of the width, height and spacing of the electrodes and the angular frequency of the applied potential wave on the pumping velocity obtained within the micro-channel. The optimal frequency of the traveling-wave potential used to induce a pumping effect within the micro-channel was found to be approximately 1 kHz irrespective of the width, height or spacing of the electrodes within the electrode array. In addition, a larger critical electrode height with a larger spacing size was required to reach the maximum pumping velocity. Also, even when the geometric ratio between the spacing and the width of the electrodes was equivalent, a larger critical height was required with a smaller width to reach its maximum pumping velocity. Furthermore, with a smaller width and a larger spacing to width ratio, the pumping velocity increased more with a larger height compared with a larger width and larger spacing to width ratio.

(Received December 6, 2010; accepted February 2, 2011)

Keywords: Traveling-Wave Potential, Electrode Arrays, Electrode Dimension, Pumping Velocity

1. Introduction

‘‘Lab-on-a-chip’’ devices or micro total analysis systems (μTAS) require precise control and manipulation of tiny volumes of fluids in small channels [1]. Traditional pressure-driven methods are not easily scaled to the micrometer regime and thus, various driving schemes have been specifically proposed for microfluidic applications [2]. Amongst the various micropumps that have been proposed, electrohydrodynamic methods, where an electrical force is applied directly to the liquid to create a pumping effect without the need for any moving mechanical parts, have gained particular attention because of their implicit simplicity, low cost, ease of fabrication, potential for integration with other microfluidic devices, etc. In general, the electrohydrodynamic phenomena exploited in such devices can be categorized as either electroosmosis [3-6], electro-wetting [7], ion-drag pumping [8] or electrohydrodynamic induction pumping [9], depending on how the fluid is activated by the external electric force.

In AC electroosmosis (ACEO) [10-12], a non-uniform ac electric field is applied to charge the electrode–electrolyte interface and generate a driving force for the accumulated electrical charges within the diffuse double layer. As a result, the liquid is subjected to a surface force,

*Corresponding author: wjluo@ncut.edu.tw

which drives the flow from regions of higher potential to regions of lower potential within the microchannel. Ajdari [13] demonstrated the theoretical feasibility of creating an ACEO-induced pumping effect that uses electrode arrays with various asymmetric configurations. Broadly speaking, two principal techniques have emerged for driving microfluidic flows: using coplanar electrode arrays, such as asymmetric electrode pairs subjected to a common ac signal [14,15], or arrays of electrodes of equal width subjected to a traveling-wave potential with four phases (TWEO) [16,17]. Of these two techniques, García-Sánchez et al. [18] demonstrated that the TWEO method is more efficient because a higher velocity was achieved with a lower voltage. However, the optimum design of the microelectrode structure is still a matter of debate [19]. For example, experimental evidence has shown that planar electrode structures achieved higher velocities simply by increasing the voltage; however, undesirable effects, including electrolysis, electrode degradation and hydrodynamic instabilities, have been observed when the voltage was increased beyond a certain critical value. Thus, in practice, the design of the microelectrode structure must be optimized in such a way as to maximize the pumping velocity whilst reducing the magnitude of the applied voltage.

Recent theoretical and experimental studies [20, 21] have shown that the pumping effect induced by an asymmetric electrode array can be improved by using a 3-D rather than a coplanar electrode structure. Urbanski et al. [22] experimentally investigated the effect of the step height on the pumping velocity induced by asymmetric pairs of 3-D electrodes and compared the results with those obtained from a simulation model. Though the simulation model failed to capture all the details of the experimentally- observed flow phenomena, the authors did conclude that a numerical model is a powerful tool to optimize the electrode configuration by to maximizing the pumping velocity. García-Sánchez et al. [23] demonstrated theoretically that the net pumping velocity induced by a TWEO array can be increased by as much as 2.7 times if the electrodes are patterned with a 3-D rather than a 2-D structure. This outcome is expected because when electrical stresses are applied to the electrolyte at the electrode–electrolyte interface, the no-slip boundary condition in the inter-electrode regions of the electrode array has a significant effect on the flow velocity within the microchannel, when the electrodes are in a coplanar structure. However, when the electrodes are patterned with a 3-D structure, the viscous friction effect is significantly reduced, and thus the flow velocity is increased. Olesen et al. [24] and Ramos et al. [25] developed theoretical models to examine the effects of faradaic currents on the TWEO phenomena observed in the linear regime. The results obtained from the models were in good qualitative agreement with those obtained from the blocking electrode model.

Despite the many contributions from the aforementioned theoretical and experimental studies, the detailed interactions between the geometry of the 3-D TWEO microelectrode structure and the resulting fluid flow phenomena are still not fully understood. Consequently, this study performed a series of numerical simulations to investigate the pumping performance of TWEO micropumps containing 3-D electrode arrays patterned on only the lower surface of a microchannel. The simulations took into account the effects of the width, height and spacing of the electrode and the frequency of the applied potential wave on the pumping velocity obtained within the microchannel containing a single-sided electrode array. The simulation results provide useful insights into the optimal design parameters and operating conditions of micropumps containing single-sided microelectrode arrays.

2. Theoretical analyses

Figure 1 illustrates the configuration of the one-sided microelectrode array considered in the initial series of simulations. As shown, the simulation model was comprised of an infinite periodic array of electrodes patterned on an insulating substrate (glass). The electrodes were considered to be infinitely long with a width d_1 and a spacing d_2. Four ac signals of amplitude V, angular frequency ω and phases 0^0, 90^0, 180^0 and 270^0, respectively, were applied to the array in such a way that the voltage acting on each electrode was phase shifted by 90^0 relative to that acting on its neighbors. A symmetrical electrolyte, e.g., KCL, was then injected into the microchannel and was driven toward the outlet via the TWEO effect induced by the electrodes. The electrode array was symmetrical in the transverse direction, about the centerline of the microchannel, and thus the 3-D simulation model reduced to a simple 2-D representation. In addition, it was assumed that the voltage applied to the electrodes was sufficiently low that

electrolysis did not occur. Finally, the frequency of the applied voltage signal was constrained, such that $\omega << \sigma / \varepsilon$, where ω is the angular frequency of the applied electric potential, σ is the conductivity and ε is the permittivity of the electrolyte. Under these conditions, the double layer acted as an ideal capacitor and resided within a quasi-equilibrium state. The electric potential acting on the electrolyte is given by $\phi = Re[\Phi exp(i\omega t)]$, where *Re* is the real part of the complex number, $\Phi exp(i\omega t)$, and Φ is a phasor that satisfies the Laplace equation, i.e.,

$$\nabla^2 \Phi = 0 \tag{1}$$

The simulation procedure began by computing the electric potential distribution throughout the entire domain, and then the corresponding electroosmotic velocity at the electrode surface was derived. In the present simulations, the Debye length, λ_D, was on the order of $10\ nm$ and was negligibly small compared with the other lengths in the system and so, its effects were neglected. Then, the ac electroosmotic flow distribution was solved by taking into account the slip boundary condition at the electrode surface, using the Helmholtz– Smoluchowski formula [26].

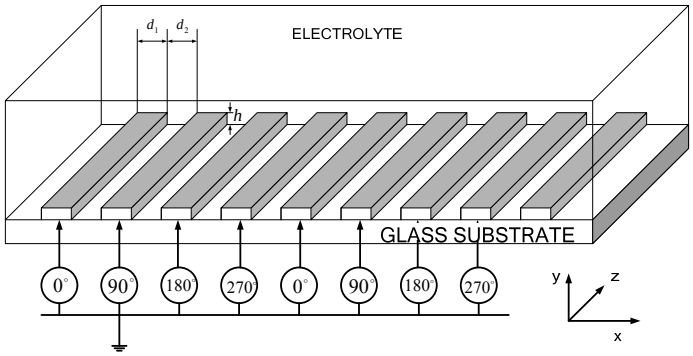

Fig. 1. Microelectrode array patterned on the lower surface of a microchannel.

2.1 Electrostatic problem

The phasor of the electric potential, Φ, can be written as $\Phi_1 + \Phi_2$, where Φ_1 and Φ_2 are the solutions to the two problems shown in Figs. 2(a) and 2(b), respectively. This approach required the Laplace equation to be solved twice but was advantageous because the size of the computational domain was reduced by a factor of eight. The boundary condition on the electrode surface described the charging of the double layer due to the current in the bulk flow, i.e., $\partial q_s / \partial t = -\sigma(\vec{n} \cdot \nabla \Phi)$, where q_s is the charge per unit area in the double layer, and $\vec{n}$ is the unit vector normal to the electrode surface. Given a sufficiently low voltage across the diffuse layer (i.e.,. $\Delta\Phi < k_B T / e$, where k_B is the Boltzmann constant, T is the absolute temperature, and e is the charge of an electron), a linear relationship exists between the surface charge and the voltage drop across the double layer. The resulting polarization of the electrode–electrolyte interface can be modeled by means of a surface impedance (*Z*). The general boundary condition at the electrode surface is then given by

$$\Phi - \sigma\, Z(\vec{n} \cdot \nabla \Phi) = V_j, \tag{2}$$

where σ is the liquid conductivity, and V_j denotes the voltage applied to the jth electrode. In this study, the surface impedance, *Z*, was modeled using the capacitor model for perfectly blocking electrodes, i.e., $Z = 1/i\omega C_{DL}$. For a negligible Stern layer, C_{DL} is estimated from the Debye–Huckel theory as $C_{DL} = \varepsilon / \lambda_D$, where λ_D is the Debye length and is related to the diffusion coefficient by $\lambda_D = \sqrt{D\varepsilon/\sigma}$. Note that the present simulations assumed that the faradaic currents reduced to zero, and thus the effects of the faradaic charge were neglected. A similar boundary condition was imposed at the interface between the electrolyte and the glass walls of the microchannel. However, for frequencies where $\omega << \sigma / \varepsilon$, the boundary condition corresponded to a zero normal current, i.e., $\vec{n} \cdot \nabla \Phi = 0$. At a boundary condition of $y \to \infty$, the potential

tended toward zero at the free surface.

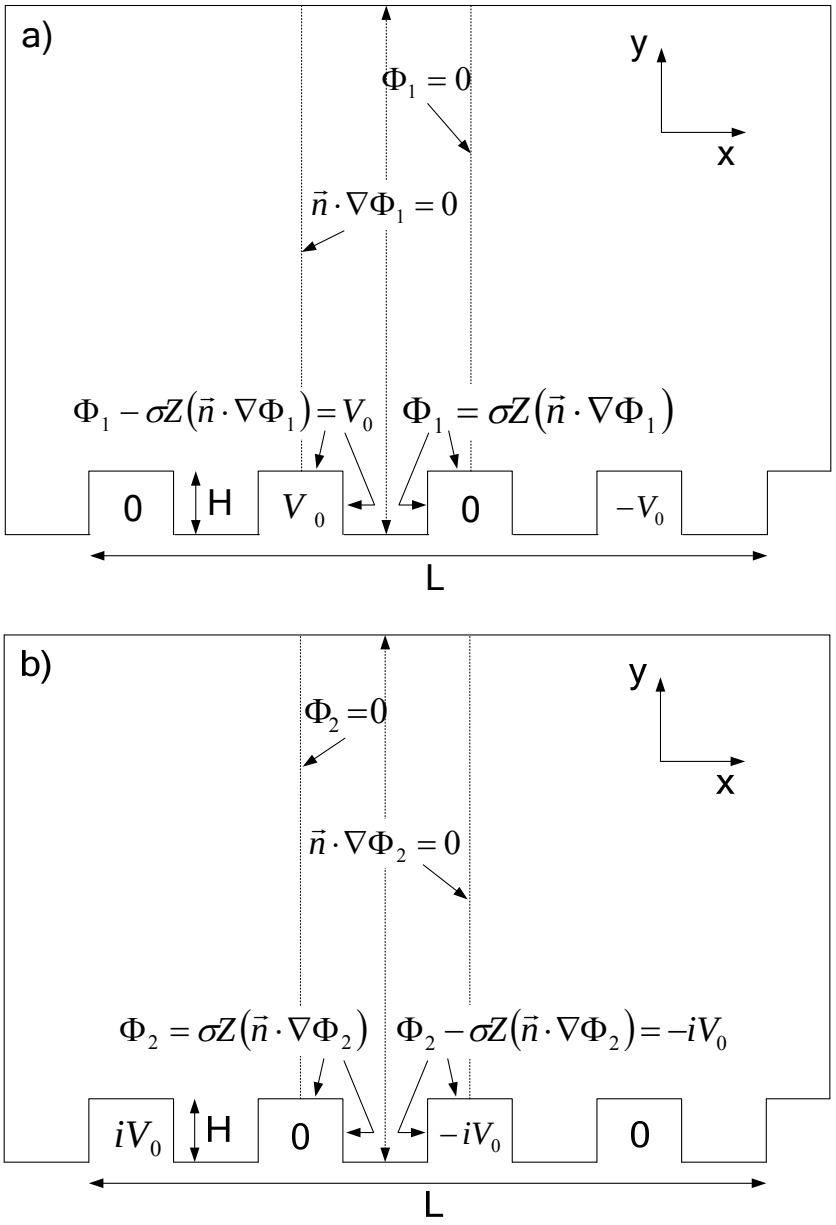

Fig. 2. Boundary conditions for the electrostatic problem.

2.2 Fluid dynamic problem

In the absence of volume forces, the fluid velocity in the microchannel is governed by the Navier-Stokes equations,

$$\frac{\partial u}{\partial x} + \frac{\partial v}{\partial y} = 0 \tag{3}$$

$$\rho\left(u\frac{\partial u}{\partial x} + v\frac{\partial u}{\partial y}\right) = -\frac{\partial p}{\partial x} + \mu\left(\frac{\partial^2 u}{\partial x^2} + \frac{\partial^2 u}{\partial y^2}\right) \tag{4}$$

$$\rho\left(u\frac{\partial v}{\partial x}+v\frac{\partial v}{\partial y}\right)=-\frac{\partial p}{\partial y}+\mu\left(\frac{\partial^2 v}{\partial x^2}+\frac{\partial^2 v}{\partial y^2}\right) \tag{5}$$

where u and v are the velocity components in the x- and y-directions, respectively, ρ is the density, μ is the viscosity, and p is the pressure. In the present simulations, Eqs. (3-5) were solved based on the following boundary conditions:

1. At the electrode surface: the diffuse double layer was considered to be in a quasi-equilibrium condition, and the electrodes were assumed to have a perfectly polarizable metal surface. Thus, the slip velocity was given as the time-based average of the Helmholtz–Smoluchowski electroosmotic velocity, u_{eo} [24],

$$u_{eo}=\frac{\varepsilon}{\eta}\left\langle \xi E_t \right\rangle$$

where ξ is the zeta potential, i.e., the voltage drop across the diffuse layer at the electrode–electrolyte interface, and E_t is the component of the electric field tangent to the electrode. The time-averaged electroosmotic velocity can be expressed in terms of the phasor of the electric potential, Φ, as follows:

$$u_{eo}=-\frac{\varepsilon}{2\eta}\Lambda\, Re\left[\left(\Phi-V_j\right)\nabla\Phi^*\cdot\vec{t}\right], \tag{6}$$

where η is the fluid viscosity, $\vec{t}$ is a unit vector tangent to the electrode surface, and Λ is the ratio of the diffuse double-layer voltage to the total double-layer voltage. Note that the normal velocity at the electrode surface was zero.

2. At the glass/electrolyte interface: the potential drop across the diffuse double layer was small, and from Eq. (6), the electroosmotic velocity on the glass was negligible (i.e., a no-slip condition was imposed).

3. Furthermore, periodic boundary conditions were imposed at the left and right boundaries in Figure 2. For the microchannel with an electrode array patterned on the lower surface only, the upper channel surface was a free surface and was located at a distance from the lower electrode array that was much greater than the characteristic size of either the electrode structure or the resulting flow vortexes. Finally, the velocity at the free surface ($\vec{u}=u\vec{e}_x$ with $\partial u/\partial y=0$) represented the net pumping velocity induced by the microelectrode array.

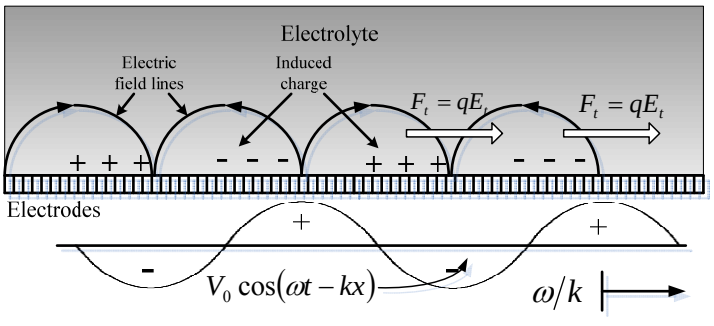

Fig. 3. Traveling-wave potential applied to the electrode array.

3. Results and discussion

3.1 AC electroosmotic flow induced by a single-sided electrode array with equal electrode width and electrode spacing in length

The simulations conducted in this study were performed using the commercial COMSOL Multiphysics package based on the physical quantities summarized in Table 1. In performing the simulations, as shown in Figure 1, four AC signals ($V(t) = V_0 \cos \omega t$) with a phase shift of 90^o were applied to every four electrodes in each array. The amplitude of the ac signals was specified as 1 V in every case, to minimize the Joule heating effect, and the voltage acting on consecutive electrodes was phase shifted by 90^0 such that a traveling-wave potential was applied to the microelectrode array, as shown in Figure 3. Applying an external electric field to the electrode array induced the formation of an electrical double layer at the interfaces between the electrodes and the electrolyte and the electrolyte and the glass surface, respectively. The applied electrical signal resulted in the accumulation of ions within the double layer. As shown in Figure 4, the external electric field acted on the charge induced in the double layer and created a driving force that pulled the fluid in the direction of the traveling wave.

Table 1. The physical parameters used in this study

d_1	Electrode width	m
d_2	Spacing of electrodes	m
V_0	Amplitude of the applied ac electric potential	$Volt$
ω	Angular frequency of the applied ac electric potential	Hz
λ_D	Debye length of the electric double layer	m
σ	Conductivity	s/m
ε	Permittivity	7.0832×10^{-10}
ϕ	Electric potential	$Volt$
Φ	Phasor of the electric potential	$Volt$
q_s	Charge per unit area in the double layer	C
k_B	Boltzmann constant	$1.38 \times 10^{-23}\ J/K$
T	Absolute temperature	$298.16K$
e	Charge of an electron	$1.6021 \times 10^{-19}\ C$
V_j	Voltage applied to the j^{th} electrode	$Volt$
Z	Surface impedance	Ohm
E_t	Component of the electric field tangent to the electrode	
C_{DL}	Capacitance per unit of area of the total double layer	
u	Velocity in the x-direction	m/s
v	Velocity in the y-direction	m/s
P	Pressure of the fluid	N/m^2
μ	Viscosity of the fluid	$0.9 \times 10^{-3}\ N \cdot s/m^2$
ρ	Density of the fluid	$10^3\ kg/m^3$
u_{eo}	Time-averaged electroosmotic velocity	m/s
ξ	Zeta potential	$Volt$
$\vec{t}$	Unit vector tangent to the electrode surface	
U	Pumping velocity	m/s
h	Electrode height	m

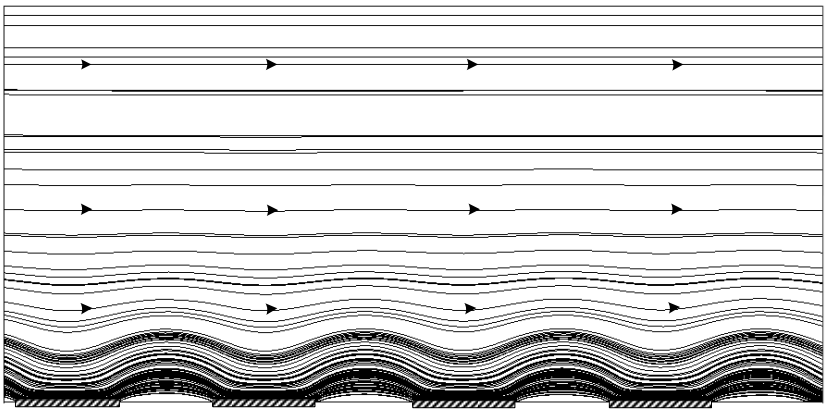

Fig. 4. Flow field induced by the traveling-wave potential.

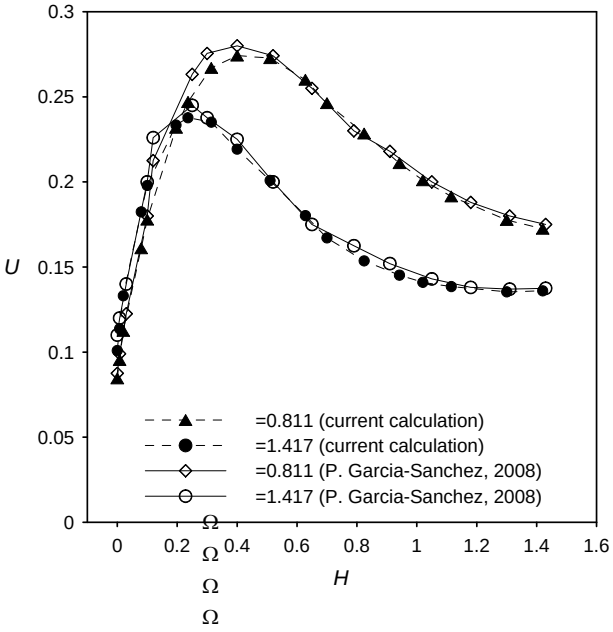

Fig. 5. Variation of the non-dimensional pumping velocity with electrode height at various values of angular frequency.

Figure 5 illustrates the variation of the non-dimensional pumping velocity, U, as a function of the non-dimensional electrode height, *H*, for a constant electrode width and electrode spacing of $d_1 = d_2 = 12.5\,\mu m$ and two different values of the non- dimensional angular frequency ($\Omega = \omega\varepsilon / \sigma\lambda_D k_0$). Note that the pumping velocity is defined as $U = \frac{1}{L}\int_0^L u\,dx$ and has units of $\Lambda\varepsilon k_0 V_0^2 / 4\eta$, where $k_0 = 2\pi / L$, and *L* is the spatial period of the system and is given by $L = 4d_1 + 4d_2$. Finally, the non-dimensional electrode height was defined as $H = k_0 h$, where h is the actual electrode height. The pumping velocity shown in Figure 5 represents the average velocity generated by the raised electrode arrays and is comparable with the net velocity induced by a planar electrode structure. The results presented in Figure 5 demonstrate that the pumping velocity was highly sensitive to the electrode height. From inspection, the maximum pumping velocity was obtained at a dimensionless electrode height of $H \approx 0.4$ for both values of the non-dimensional angular frequency $\Omega = 0.811$ and $\Omega = 1.147$ ($\Omega = \omega\varepsilon / \sigma\lambda_D k_0$). In other words, the optimal value of the electrode height was approximately $10.4\,\mu m$. The maximum velocity obtained in the microchannel with raised electrodes was approximately 2.7 times higher than that obtained when using a planar microelectrode structure (i.e., *H*=0). This performance improvement reflects a reduction in viscous friction acting on the fluid in the

electrode gap as the height of the electrode structure was increased. Finally, it was observed that for both values of the dimensionless angular frequency, the simulation results were in agreement with the numerical findings presented by García-Sánchez [15]. Thus, it was inferred that our numerical results were reliable and can be used to further investigate the flow conditions in the microchannel.

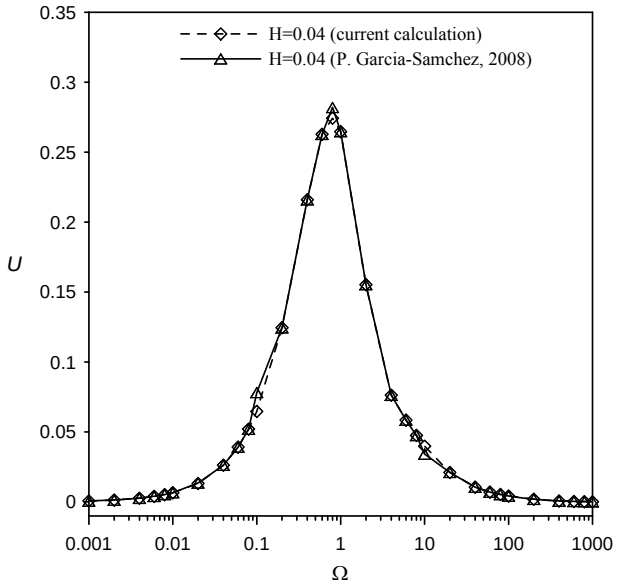

Fig. 6. Variation of the pumping velocity with angular frequency for a constant electrode height of 10.4 μm.

Figure 6 plots the variation of the non-dimensional pumping velocity (U) with the angular frequency (Ω) for a constant electrode height of $10.4\mu m$ ($H \approx 0.4$). It can be seen that the maximum velocity was obtained at a frequency of approximately $1\ kHz$. Again, the present results were in good agreement with those presented by García-Sánchez [15].

3.2 AC electroosmotic flow induced by a single-sided electrode array with unequal electrode width and electrode spacing in length

To investigate the effects of the width, height and spacing of the electrode and the frequency of the applied potential wave on the pumping velocity, the following dimensionless parameters were defined:

$$R = d_2/d_1,\ \ H^* = h/d_1,\ \ U^* = u/\left(\Lambda\varepsilon\ d_1/\eta\right),\ \ \Omega = \omega\varepsilon/\sigma\lambda_D k_0.$$

Figure 7 illustrates the variation of the pumping velocity with the angular frequency (Ω) for a constant electrode height and various values of the width (d_1) and spacing-electrode width ratio, R. It was observed that in every case, the maximum velocity was obtained when the electrodes were actuated at approximately $1\ kHz$, irrespective of the width, height or spacing of the electrodes within the electrode array. Figure 8 plots the pumping velocity against the electrode spacing-width ratio for different widths. In the figure, the electrode height and angular frequency were $10.4\mu m$ and $1\ kHz$, respectively. For a constant electrode height (i.e., $10.4\mu m$) and the same electrode width, the pumping velocity increased as the electrode spacing-width ratio decreased. For a given area of the micro-channel surface, a smaller electrode width-spacing ratio generated a larger electrode area in the micro-channel, and more ions above the electrode surface were induced by the traveling-wave potential. Thus, the results presented in Figure 8 show that for a given electrode height and applied frequency, the pumping velocity gradually increased as the

electrode spacing decreased because of the greater number of accumulated ions in the double layer above the electrode surface. Moreover, it was also seen that for a constant electrode width and at the same electrode spacing-width ratio, the pumping velocity was also greatly affected by the electrode height.

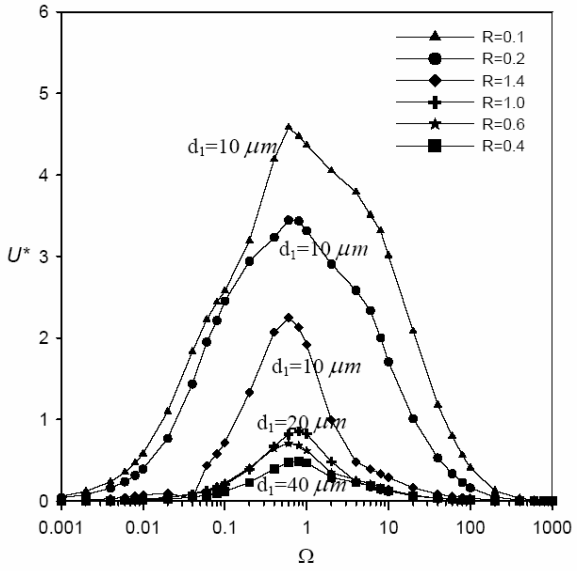

Fig. 7. Variation of the pumping velocity with angular velocity (Ω) for various values of the electrode width and electrode spacing-width ratio. Note that the electrode height was $10.4\mu m$.

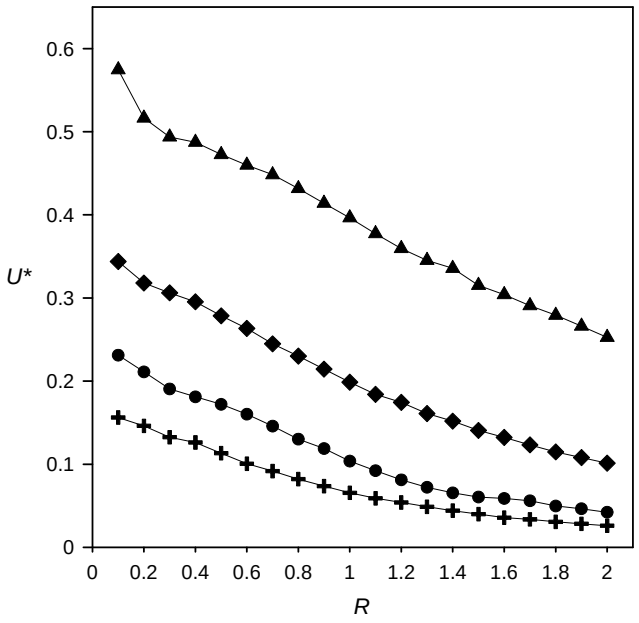

Fig. 8. Pumping velocity against different electrode spacing-width ratios. Note that the electrode height was $10.4\mu m$.

Figures 9(a-c) show the variation of the pumping velocity with the electrode heights for electrode widths of $d_1 = 40\mu m$, $20\mu m$ and $10\mu m$ under the influence of various electrode spacing-width ratios. Note that the frequency of the applied traveling-wave potential was $1\ kHz$ in every case. Figure 9(a) shows that when the electrode width and the electrode spacing size were both kept constant, the pumping velocity reached a maximum value at a critical electrode height (H_c). For the case of R=0.2 in Figure 9(a), the electrode spacing size was much smaller than the electrode width, and the corresponding H_c was approximately 0.15. However, for the case of R=2 in Figure 9(a), the electrode spacing size was much larger than the electrode width, and the corresponding H_c was approximately 0.25. This phenomenon indicates that if the electrode width is kept constant, the maximum pumping velocity will gradually decrease with an increase in the electrode spacing because of the increase in viscous friction, but the corresponding H_c will gradually increase. In other words, with a larger spacing size, a larger critical electrode height (H_c) will be required to reach its maximum pumping velocity. Otherwise, as seen by comparing Figures 9(a-c), the value of H_c ranged between 0.15 and 0.25 when an electrode width of 40 μm was used, and the R value increased from 0.2 to 2. However, for the cases with electrode widths of 20 μm and 10 μm, the corresponding H_c was between 0.25 and 0.55 and 0.55 and 1.1, respectively. This phenomenon indicates that if the geometric ratio of the electrode spacing to electrode width is equivalent (i.e., R is the same), a larger H_c is required for a smaller electrode width to reach its maximum pumping velocity. Furthermore, with a smaller electrode width and large electrode spacing to electrode width ratio, the pumping velocity was increased more when the electrode height was increased compared with when the electrode width and electrode spacing to electrode width ratio was increased.

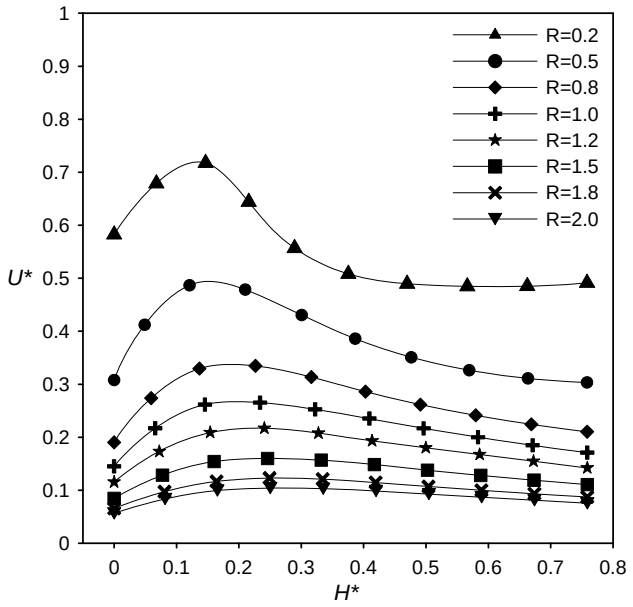

Fig. 9(a) Variation of the pumping velocity with electrode spacing-width ratio for different electrode heights. Note that the electrode width was 40 μ m, and the angular frequency was 1 kHz.

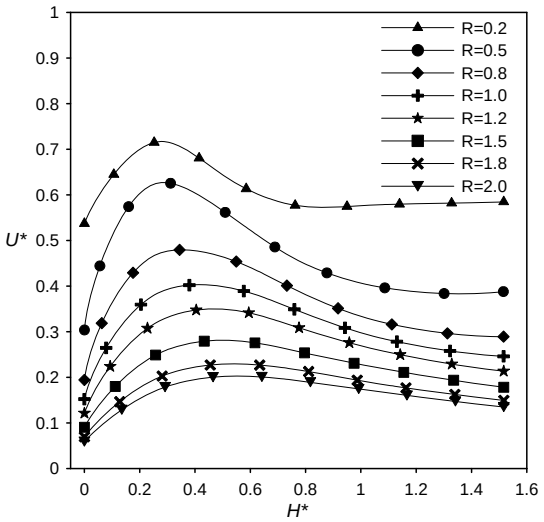

Fig. 9(b) Variation of the pumping velocity with an electrode spacing-width ratio for different electrode heights. Note that electrode width was 20 μ m, and the angular frequency was 1 kHz.

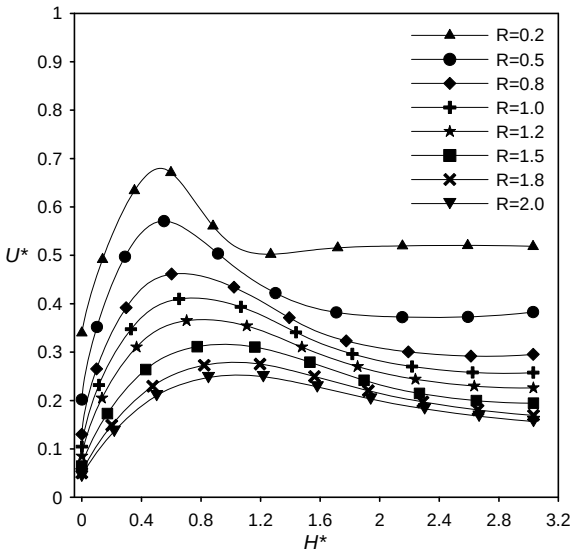

Fig. 9(c) Variation of the pumping velocity with electrode spacing-width ratio for different electrode heights. Note that electrode width was 10 μ m, and the angular frequency was 1 kHz.

4. Conclusions

This study performed a series of numerical simulations to investigate the pumping performance of micro-pumps that contained a single electrode array patterned on the lower surface of a micro-channel. It was shown that the optimal frequency of the traveling-wave potential used to induce a pumping effect within the micro-channel was approximately 1 kHz, irrespective of the width, height or spacing of the electrodes within the electrode array. In addition, the results also showed that for a given electrode height and applied frequency, the pumping velocity gradually increased as the electrode spacing was reduced because of a greater number of accumulated ions in the double layer above the electrode surface. Finally, it was shown that with a larger spacing size, a larger critical electrode height (H_c) was required to reach its maximum pumping velocity. If the

geometric ratio of the electrode spacing to electrode width was equivalent (i.e., R is the same), a larger H_c was required with a smaller electrode width to reach its maximum pumping velocity. Furthermore, with a smaller electrode width and large electrode spacing to electrode width ratio, the pumping velocity was increased more when the electrode height was increased compared with when the electrode width and high electrode spacing to electrode width ratio was increased.

Acknowledgments

The authors gratefully acknowledge the financial support provided for this study by the National Science Council of Taiwan under Grant Nos. NSC 98-2218-E-167-001 and NSC 98-2221-E-167-017-MY2.

References

[1] H. Stone, A. Stroock, A. Ajdari, Annu. Rev. Fluid Mech. **36,** 381411 (2004).
[2] D.J. Laser, J.G. Santiago, J. Micromech. Microeng. **14**, R35 (2004).
[3] V. Pertorius, B. Hopkins, J. Schieke, J. Chromatogr. **99**, 23 (1974).
[4] W.J. Luo, Microfluid Nanofluid, **6**, 189 (2009).
[5] K.F. Yarn,; S.P. Hsu,; W.J. Luo,; H.J. YE, Science in China Series G: Physics Mechanics Astron, **52**, 602 (2009).
[6] W.J. Luo, K.F. Yarn, S.P. Hsu, Jpn. J. Appl. Phys. **46**, 1608 (2007).
[7] G. Beni, M. Tenan, J. Appl. Phys. **52**, 6011 (1995).
[8] A. Richter, H. Sandmaier, IEEE Proceedings of micro electro mechanical systems. New York, 99 (1990).
[9] G. Fuhr, R. Hagedorn, T. Muller, W. Benecke, B. Wagner, J. Micro Electro mech. Syst. **1**, 141 (1992).
[10] A. Ramos, H. Morgan, N. Green, A. Castellanos, J. Colloid Interface Sci. **217**, 420 (1999).
[11] N. Green, A. Ramos, A. González, H. Morgan, A. Castellanos, Phys. Rev. E **61**, 4011 (2000).
[12] A. González, A. Ramos, N. Green, A. Castellanos, H. Morgan, Phys. Rev. E **61**, 4019 (2000).
[13] A. Ajdari, Phys. Rev. E **61**, R45 (2000).
[14] A.B.D. Brown, C.G. Smith, A.R. Rennie, Phys. Rev. E **63**, 016305 (2000).
[15] V. Studer, A. Pe´pin, Y. Chen, A. Ajdari, Analyst **29**, 944 (2004).
[16] B.P. Cahill, L.J. Heyderman, J. Gobrecht, A. Stemmer, Phys. Rev. E **70**, 036305 (2004).
[17] A. Ramos, H. Morgan, N. Green, A. González, A. Castellanos, J. Appl. Phys. **97**, 084906 (2005).
[18] P. García-Sánchez, A. Ramos, N. Green, H. Morgan, IEEE Trans. Dielectr. Electr. Insulat. **13**, 670-677 (2006).
[19] L. Olesen, H. Bruus, A. Ajdari, Phys. Rev. E **73**, 056313 (2006).
[20] M.Z. Bazant, Y. Ben, Lab Chip **6**, 1455 (2006).
[21] J.P. Urbanski, T. Thorsen, J.A. Levitan, M.Z. Bazant, Appl. Phys. Lett. **89**, 143508 (2006).
[22] J.P. Urbanski, J.A. Levitan, D.N. Burch, T. Thorsen, M.Z. Bazant, Colloid Interface Sci. **309**, 332 (2007)
[23] P. García-Sánchez, A. Ramos, Microfluid. Nanofluid. **5**, 307 (2008).
[24] L. Olesen, PhD Thesis, Technical University of Denmark (2006).
[25] A. Ramos, A. González, P. García-Sánchez, A. Castellanos, J. Colloid Interface Sci. **309**, 323 (2007).
[26] N. Green, A. Ramos, A. González, H. Morgan, A. Castellanos, Phys. Rev. E **66**, 026305 (2002).